Carbon Trends 13 (2023) 100318

Contents lists available at ScienceDirect

Carbon Trends

journal homepage: www.elsevier.com/locate/cartre

Laser writing of preferentially orientated nitrogen-vacancy centers in diamond

Kohei Kinouchi [a], Yasuhiko Shimotsuma [a,*], Mitsuharu Uemoto [b], Masanori Fujiwara [c], Norikazu Mizuochi [c,d], Masahiro Shimizu [a], Kiyotaka Miura [a]

[a] Department of Material Chemistry, Kyoto University, Kyotodaigaku-Katsura, Kyoto, 615-8510, Japan
[b] Department of Electrical and Electronic Engineering, Kobe University, Nada, Kobe, 657-8501, Japan
[c] Institute for Chemical Research, Kyoto University, Uji, Kyoto, 611-0011, Japan
[d] Center for Spintronics Research Network, Kyoto University, Uji, Kyoto, 611-0011, Japan

ARTICLE INFO

Keywords:
Femtosecond laser processing
Polarization
NV center
Diamond
First-principle calculation

ABSTRACT

Nitrogen-vacancy centers in diamond have gained widespread attention as quantum systems that can be applied in quantum information devices. The excellent properties of quantum devices can be enhanced using preferentially oriented nitrogen-vacancy (NV) centers. However, thus far, orientation control has been achieved only via chemical vapor deposition. In this study, we demonstrate the creation of preferentially oriented NV centers via laser writing. The alignment ratio of ensemble NV centers is biased along the direction parallel to [111], depending on the femtosecond laser polarization, causing an increase of 55 % in contrast to the optically magnetic resonance signal at maximum compared with 25 % in random orientation. Based on time-dependent density-functional theory (TDDFT) simulations and experimental observations, such complex polarization dependence can be attributed to the anisotropy of electron excitation. This technique provides a new optical fabrication method for engineered materials and devices used in quantum technology.

1. Introduction

Nitrogen-vacancy (NV) centers, composed of nitrogen impurities adjacent to a vacancy in diamond, have attracted interest for application in quantum devices such as qubits [1]. The NV center trapping an electron is called NV^- center and has a long spin coherence time at room temperature [2]. Moreover, its spin states can be optically detected and controlled. Unlike a single NV center that is usually applied in high-resolution quantum sensors [2], quantum computing [3], and single-photon sources [4] used in quantum cryptographic communication [5], ensemble NV centers are applicable to ultrahigh-sensitivity quantum sensors [6] for monitoring magnetic and electric fields, temperature, and stress. The number of NV spins (n_{NV}), ensemble spin coherence time (T_2), and readout contrast (C) are the three crucial factors determining the sensitivity of a magnetic field detected by ensemble NV centers [7]. Although the ideal sensitivity is inversely proportional to the square root of n_{NV} and T_2, an optimal n_{NV} (10^{15}–10^{18}) exists [7]. Furthermore, from the viewpoint of many-body physics, T_2 decreases with an increase in n_{NV} [8]. In particular, the preferential orientation of the ensemble NV centers in four equivalent diamond crystallographic axes improves the readout contrast [9].

The conventional techniques for creating high-density NV center ensembles include electron-beam irradiation [10] and nitrogen-ion implantation [11]. However, in these methods, the distribution of NV centers in the beam irradiation direction varies [12]. Although high-orientation NV centers can be formed by nitrogen-doped CVD homoepitaxial growth on (111) diamond substrate [13], it is impossible to rearrange the directions of the NV axes after crystal growth. Recently, Chen et al. reported a single NV formation via femtosecond laser irradiation followed by thermal annealing [14] as a possible technique to overcome these drawbacks. They also observed the axial statistical distribution of a single NV center using fluorescence measurements during laser annealing [15]. In this photoinduced method, the NV formation mechanism is presumed to be as follows: first, a vacancy is formed owing to nonlinear optical effects; second, the vacancy migrates under thermal treatment; finally, it binds to the substitutional nitrogen [15]. The advantages of this technique include the non-destructive and space-selective formation of NV centers via multiphoton absorption and

* Corresponding author.
E-mail address: shimotsuma.yasuhiko.3m@kyoto-u.ac.jp (Y. Shimotsuma).

https://doi.org/10.1016/j.cartre.2023.100318
Received 12 October 2023; Received in revised form 4 December 2023; Accepted 4 December 2023
Available online 5 December 2023

its ability to manipulate NV centers in diamond for the desired application after crystal growth. More recently, we also demonstrated the highly efficient formation of ensemble NV centers by optimizing laser parameters such as pulse width, pulse energy and number of pulses [16,17]. We also confirmed the formation of NV centers after single-pulse irradiation without heat treatment [18,19].

As the vacancy migrates isotropically during the aforementioned thermal process, the formation and migration of vacancies by the laser polarization direction can be controlled via nonlinear optical phenomena, such as multiphoton absorption, which is similar to NV formation [20]. The dominant light-matter interaction changes from linear to nonlinear interaction such as multiphoton absorption and tunnel ionization, depending on the laser intensity [21,22]. More interestingly, theoretical studies have shown that the effect of multiphoton absorption depends on the polarization state [23]. It is also known that the ionization efficiency of gases such as N_2 and O_2 depends on the linear polarization direction [24]. Moreover, in the case of solid materials, the transmittance [25] and absorbance [26] depend on the polarization direction, even for optically isotropic materials, such as lithium fluoride crystals. Such anisotropic phenomena are caused by the relative angle between the molecular or crystal axis and the electric field direction; this has been interpreted in terms of the anisotropy of the effective mass [25] or the third-order nonlinear susceptibility tensor $\chi^{(3)}$ [26]. Another polarization-dependent anisotropic phenomenon in isotropic materials such as glass [27,28] also originates from the quantum interference of multiphoton absorption, resulting from the asymmetry of photoionization based on the model of the coherent photovoltaic effect proposed by Dianov et al. [29].

Although these findings indicate that vacancy formation in the diamond structure depends on the polarization direction, the relaxation of hot electrons, and energy transfer to the lattice, followed by vacancy migration and its binding to substitutional nitrogen, should also be affected by the polarization direction. If the number of pulses is quite small and the laser pulse width is shorter than the time required for NV formation in the region close to the defect sites, the orientation of the NV axis may also be affected by the direction of the electric field. In this study, we performed first-principle calculations to simulate the response of a diamond crystal structure excited by an intense electric field. Further, we investigated the possibility of polarization-dependent electronic excitation states. In addition, we experimentally demonstrated that the degree of the NV axis orientation aligned to [111] changed with the polarization direction.

2. Methods

2.1. Time-Dependent density-functional theory (TDDFT) calculation methods

In the TDDFT simulation, the open-source TDDFT program package, SALMON (Scalable Ab Initio Light-Matter Simulator for Optics and Nanoscience) [35] was used, and a norm-conserving pseudopotential [36] was employed for electron-ion interactions. The adiabatic local density approximation (ALDA) with the Perdew-Zunger functional [37] was adopted for the exchange-correlation potential. In the simulation, we used a unit cell including 8 carbon atoms and set the periodic boundary condition. For the coordinate system, a unit grid with a cubic crystal in a uniform Cartesian coordinate system and a diamond structure with a lattice constant of 3.57 Å were prepared; further, eight carbon atoms were spatially arranged in a system with a grid size of $Dx = Dy = Dz = 0.18$ Å, which were spatially divided into 20 × 20 × 20 sections in real space. The number of k-points N_k and the time step size dt were set to 12^3 and 0.48 attosecond (as), respectively. The external electric field was described as an intense pulse with a peak power density from 1.0×10^{12} to 1.0×10^{14} W/cm^2 and a pulse continuing time ($\neq$ FWHM = 11 fs) of 30 fs. Owing to computational constraints, the pulse width was different from that in the experiments (50 fs). The direction of the electric field oscillating in the (111) plane, corresponding to the linear polarization direction θ was set as 0° at $[\overline{1}12]$. This direction was rotated from 0° to 60° (2° intervals) in a positive counterclockwise direction, as seen from [111]. To investigate the interaction between the diamond crystal and the intense electric field with different directions to the crystal axis, the number of excited electrons $n_{\mathrm{ex}}(t,\ \theta)$ at the elapsed time t was calculated using Eq. (1). It should be noted that the values obtained from the following equations are values per unit cell volume.

$$n_{\mathrm{ex}}(t,\ \theta) = \frac{1}{N_k}\sum_{\mathbf{k}}\sum_{b\in \mathrm{CB}} P_{b\mathbf{k}}(t) \tag{1}$$

with

$$P_{b\mathbf{k}}(t) = 2\sum_{b'\in \mathrm{occ}} \left| \left\langle u^0_{b\mathbf{k}+\mathbf{A}(t)/c}(\mathbf{r}) \middle| u_{b'\mathbf{k}}(\mathbf{r},t)\right\rangle \right|^2 \tag{2}$$

where $\mathbf{A}(t)$ and c are the vector potential and the speed of light, respectively. $u(\mathbf{r})^0_{b\mathbf{k}}$ and $u_{b\mathbf{k}}(\mathbf{r},t)$ in Eq. (2) are the Bloch functions of the ground and excitation states, respectively, indexed by the band index b and wave vector $\mathbf{k}$. In Eq. (1), the $n_{\mathrm{ex}}(t,\ \theta)$ was summed over the conduction bands (CB) ($b = 17,\ 18,\ \ldots,\ 32$) and all k-points. In addition, in Eq. (2), the $P_{b\mathbf{k}}(t)$ was also summed over the bands occupied by electrons (occ), where we used the Houston state $u^0_{b\mathbf{k}+\mathbf{A}(t)/c}(\mathbf{r})$ as the reference state of the projection to define electron excitation [30,38]. The number of excited electrons in each band $n_{\mathrm{ex}}(b,\ t,\ \theta)$ was calculated using

$$n_{\mathrm{ex}}(b,t,\ \theta) = \frac{1}{N_k}\sum_{\mathbf{k}} P_{b\mathbf{k}}(t) \tag{3}$$

Furthermore, we calculated the carrier density of states (cDoS) $D_{\mathrm{p}}(E,\ t,\ \theta)$ for excited electrons and holes using Eqs. (4) and (5), respectively, to reveal the effect of an intense electric field on the excited carrier distribution in different directions.

$$D_{\mathrm{p,\ elec}}(E,t,\theta) = \frac{1}{N_k}\sum_{\mathbf{k}}\sum_{b\in \mathrm{CB}} P_{b\mathbf{k}}(t)\delta(E-\varepsilon_{b\mathbf{k}}) \tag{4}$$

$$D_{\mathrm{p,\ hole}}(E,t,\theta) = \frac{1}{N_k}\sum_{\mathbf{k}}\sum_{b\in \mathrm{VB}} [2-P_{b\mathbf{k}}(t)]\delta(E-\varepsilon_{b\mathbf{k}}) \tag{5}$$

where VB represents the valence bands. The subscripts 'elec' and 'hole' denote electron and hole, respectively. In these calculations, the reference energy was set at the Fermi level. When describing the electron density at position $\mathbf{r}$ in real space as

$$d(\mathbf{r},\ t) = \frac{2}{N_k}\sum_{\mathbf{k}}\sum_{b} |u_{b\mathbf{k}}(\mathbf{r},t)|^2 \tag{6}$$

the polarization dependence of the differences $d_{\mathrm{diff}}(\mathbf{r},\ t)$ ($\equiv d(\mathbf{r},\ t) - d(\mathbf{r},\ 0)$) from the ground state in a real-space distribution can be investigated.

2.2. Laser direct-writing of ensemble NV centers

A mode-locked regeneratively amplified Ti: sapphire laser system (Mira/RegA9000, Coherent) operating at 800 nm was used to create ensemble NVs inside the diamond samples. We used a high-pressure high-temperature (HPHT) type-Ib single crystalline (111)-oriented diamond substrate (2.0 mm × 2.0 mm × 0.5 mm, Sumitomo Electric Industries), whose concentration of neutral charge substitutional nitrogen (P1 center) was estimated to be approximately 29 ppm via FT-IR measurement. Linearly polarized laser pulses were focused through an oil-immersion objective lens (U Plan S Apo 100×, N.A. 1.40, Olympus) to a depth of 50 μm inside the diamond sample in a grid with 10 μm spacing. The laser pulse width was measured immediately before the objective lens by using a scanning interferometric autocorrelator (AA-M, Avesta). The laser irradiation conditions were set as follows: 2000

pulses, a repetition rate of 10 kHz, a pulse width of 50 fs, and a pulse energy of 200 nJ. Under these conditions, no apparent thermal accumulation leading to laser annealing occurred. The polarization direction, i.e., the azimuthal angle θ of the electric field, was rotated in the (111) plane from 0° to 120° (6° intervals) using a half-wave plate. We also performed the direct writing of ensemble NVs using femtosecond laser pulses with a circular polarization. Other conditions were set to be the same as described above. A circular polarization was generated using a quarter-wave plate. We conducted all experiments at room temperature (24 °C), and we did not perform thermal annealing.

2.3. Optical detected magnetic resonance (ODMR) measurements

To analyze the axial orientation of the ensemble NVs, ODMR measurements were performed at room temperature using a confocal microscope equipped with a 532 nm CW laser with an average power of 100 μW. An external static magnetic field of 5.6 mT parallel to [111] ($B^{\circ}\|[111]$) was applied using a permanent magnet. For electron spin resonance (ESR), a microwave field was delivered to the laser-processed regions using a thin copper wire with a diameter of 30 μm; the copper wire was strung onto the diamond surface (Supplementary Fig. S1). The details are described in a previous report [39]. Details of ODMR measurement method are shown in Supplementary Information 1. The alignment ratios along the [111] direction for the originally existing NVs obtained at the two different positions were averaged. We conducted three individual measurements following the described procedure. The typical ODMR signals for both the laser-processed region and the pristine diamond near it were presented in Supplementary Figs. S2−S7. The sums of each two ODMR signals in the direction parallel to [111] or along the other three equivalent directions ($[11\bar{1}]$, $[\bar{1}11]$, and $[1\bar{1}1]$) are obtained as $S_{[111]}$ and S_{others}.

2.4. Fluorescence polarization microscope (FPM) measurements

For the FPM measurements, we used an inhouse-built confocal microscope equipped with a 532 nm CW laser and a photomultiplier tube detector. The polarization direction ϕ for the excitation laser with an average power of 10 μW was rotated from 0° to 220° in the (111) plane of the diamond sample. Details of FPM measurement method are shown in Supplementary Information 2. The fluorescence intensities for the laser-processed region and the pristine diamond from FPM measurements are plotted in Supplementary Figs. S8−S10.

2.5. Analysis method for the ODMR signal

The orientation of the NV axes can be identified using the ODMR signals derived from the NV centers in the direction parallel to [111] or along the other three equivalent directions ($[11\bar{1}]$, $[\bar{1}11]$, and $[1\bar{1}1]$). After fitting the ODMR signals using Lorentz functions, the alignment ratio along the [111] direction $R_{[111]}(\theta)$ was calculated based on [39], as follows:

$$R_{[111]}(\theta) = \frac{S_{[111]}(\theta)}{S_{[111]}(\theta) + k(\theta)S_{\text{others}}(\theta)} \tag{7}$$

where $S_{[111]}(\theta)$ and $S_{\text{others}}(\theta)$ represent the fitted peak area of ODMR signals along the [111] and the other three axes, from NV centers induced by the femtosecond laser pulses with the polarization direction of θ. $k(\theta)$ is an empirical parameter to correct signal differences owing to the experimental setup. The detailed procedures to calculate $R_{[111]}(\theta)$ are as follows: we measured the ODMR signals at each laser-processed region (Supplementary Figs. S5−S7). Second, the normalized ODMR signals were fitted by the four Lorentz functions and obtained $S_{[111]}(\theta)$ and $S_{\text{others}}(\theta)$. Third, we used the $k(\theta)$ value to be 1.4 by considering the microwave application method [39]. Using $k(\theta) = 1.4$, we finally calculated $R_{[111]}(\theta)$ by Eq. (7).

2.6. Analysis method for the FPM signal

Further, we verified the in-plane polarization dependence of the (111) plane using FPM measurements. The measured fluorescence intensities for the laser-processed region $I_{\text{NV}}(\theta,\ \phi)$ were normalized using the value for the pristine diamond $I_{\text{bkg}}(\theta,\ \phi)$. It should be noted that the angles θ and ϕ represent the polarization direction of the femtosecond laser for NV formation and the green laser for fluorescence measurement, respectively. The fluorescence intensities for the laser-processed region $I_{\text{NV}}(\theta,\ \phi)$ and the pristine diamond $I_{\text{bkg}}(\theta,\ \phi)$ are plotted in Supplementary Figs. S8−S10. The normalized intensity, defined as $I_{\text{r}}(\theta,\ \phi)$ $(\equiv I_{\text{NV}}(\theta,\ \phi)/I_{\text{bkg}}(\theta,\ \phi))$, was plotted with respect to the polarization direction ϕ of the excitation green laser and fitted using the following function:

$$I_{\text{r}}(\theta,\ \phi) = A_0(\theta) + A_1(\theta)\cos 2[\phi - \phi_{\text{c}}(\theta)] \tag{8}$$

The following analysis was performed to verify the orientation of the NV axes. The unit vectors along the four bond axes in the diamond structure, corresponding to the possible orientations of the NV center, are defined as follows: $\mathbf{a} = \frac{1}{\sqrt{3}}(1,\ 1,\ 1)$, $\mathbf{b} = \frac{1}{\sqrt{3}}(1,\ 1,\ -1)$, $\mathbf{c} = \frac{1}{\sqrt{3}}(-1,\ 1,\ 1)$, and $\mathbf{d} = \frac{1}{\sqrt{3}}(1,\ -1,\ 1)$. Given the electric dipole moments $\boldsymbol{\mu}_{ij}$ (i= a, b, c, d, j= V, H) of NV centers, the $\boldsymbol{\mu}_{ij}$ is in the plane perpendicular to the symmetry axis of the **a**, **b**, **c**, **d** plane [40] and is the orthogonally intersecting unit vector with each other. Here, the indices, i and j, denote the direction along the symmetry axis and the orthogonally intersecting direction of 'V' and 'H', respectively. The eight electric dipole moments are as follows: $\boldsymbol{\mu}_{\text{aV}} = \frac{1}{\sqrt{6}}(-1,\ -1,2)$, $\boldsymbol{\mu}_{\text{aH}} = \frac{1}{\sqrt{2}}(-1,1,0)$, $\boldsymbol{\mu}_{\text{bV}} = \frac{1}{\sqrt{6}}(-1,-1,-2)$, $\boldsymbol{\mu}_{\text{bH}} = \frac{1}{\sqrt{2}}(1,-1,0)$, $\boldsymbol{\mu}_{\text{cV}} = \frac{1}{\sqrt{6}}(-2,-1,-1)$, $\boldsymbol{\mu}_{\text{cH}} = \frac{1}{\sqrt{2}}(0,\ 1,\ -1)$, $\boldsymbol{\mu}_{\text{dV}} = \frac{1}{\sqrt{6}}(-1,\ -2,\ -1)$ and, $\boldsymbol{\mu}_{\text{dH}} = \frac{1}{\sqrt{2}}(-1,\ 0,\ 1)$. Moreover, a unit vector parallel to an electric field can be described in this coordinate system as $\mathbf{E}(\phi) = \left(-\frac{1}{\sqrt{2}}\sin\phi - \frac{1}{\sqrt{6}}\cos\phi,\ \frac{1}{\sqrt{2}}\sin\phi - \frac{1}{\sqrt{6}}\cos\phi,\ \frac{2}{\sqrt{6}}\cos\phi\right)$.

In the case of weak excitation such as FPM, perturbation Hamiltonian H' can be approximated as $H' \approx -\boldsymbol{\mu}\cdot\mathbf{E}$ under the electric dipole approximation. As the fluorescence intensity is proportional to the density of the excited state, and this density is proportional to the number of formed ensemble NVs, the polarization-dependent fluorescence intensity $I_{\text{r}}(\theta,\ \phi)$ can be calculated by applying Fermi's golden rule. Based on this rule, the fluorescence intensity is proportional to $|\boldsymbol{\mu}_{ij}\cdot\mathbf{E}(\phi)|^2$ [41]; thus, $I_{\text{r}}(\theta,\ \phi)$ is represented as:

$$I_{\text{r}}(\theta,\ \phi) \propto \sum_{i=a,b,c,d}\sum_{j=H,V} k_i(\theta)\left|\boldsymbol{\mu}_{ij}\cdot\mathbf{E}(\phi)\right|^2 = a + \frac{5}{9}(b+c+d) + \frac{4}{9}\sqrt{A(\theta)^2 + B(\theta)^2}\cos 2\left(\phi + \frac{\alpha(\theta)}{2} - 45^{\circ}\right) \tag{9}$$

with

$$A(\theta) = -b + \frac{c+d}{2},\ B(\theta) = \frac{\sqrt{3}}{2}(-c+d),\ \tan\alpha(\theta) = \frac{A(\theta)}{B(\theta)} \tag{10}$$

where the indicator of the number of formed ensemble NVs is $k_i(\theta)$ $(= a,\ b,\ c,\ d)$, which is considered a function of θ. Comparing the fitting parameters of $A_0(\theta)$, $A_1(\theta)$, and $\phi_c(\theta)$ in Eq. (8) from the FPM measurements and the theoretical function in Eq. (9), the values in Eqs. (9) and (10) are calculated as follows:

$$\alpha(\theta) = 90^\circ - 2\phi_c(\theta) \tag{11}$$

$$A(\theta) = \frac{9}{4}A_1(\theta)\sin\alpha(\theta) \tag{12}$$

$$B(\theta) = \frac{9}{4}A_1(\theta)\cos\alpha(\theta) \tag{13}$$

Using these values, the polarization dependence of the fluorescence intensity along the four NV axes can be determined as follows:

$$a(\theta) = \frac{9A_0(\theta)R_{[111]}(\theta)}{5 + 4R_{[111]}(\theta)} \tag{14}$$

$$b(\theta) = \frac{3A_0(\theta)\left[1 - R_{[111]}(\theta)\right]}{5 + 4R_{[111]}(\theta)} - \frac{2}{3}A(\theta) \tag{15}$$

$$c(\theta) = \frac{3A_0(\theta)\left[1 - R_{[111]}(\theta)\right]}{5 + 4R_{[111]}(\theta)} + \frac{1}{3}A(\theta) - \frac{1}{\sqrt{3}}B(\theta) \tag{16}$$

$$d(\theta) = \frac{3A_0(\theta)\left[1 - R_{[111]}(\theta)\right]}{5 + 4R_{[111]}(\theta)} + \frac{1}{3}A(\theta) + \frac{1}{\sqrt{3}}B(\theta) \tag{17}$$

where $R_{[111]}(\theta)$ is the alignment ratio along the [111] direction obtained using the ODMR measurements and is expressed by the equation, $R_{[111]}(\theta) = a/(a+b+c+d)$. Finally, the polarization dependence of $r_i(\theta)$, representing the alignment ratio along the four NV axes' directions, can be individually investigated.

$$r_i(\theta) = k_i/(a+b+c+d),(k_i = a,\ b,\ c,\ d) \tag{18}$$

It should be noted that in this analysis method, we only focused on the differences in the $\boldsymbol{\mu}_{ij}$ direction owing to the different axes' orientations of ensemble NVs formed by the femtosecond laser pulses with varying polarization direction θ.

3. Results

3.1. TDDFT calculation results

We performed TDDFT calculations to investigate the possibility of polarization dependence in the electron excitation of a diamond via nonlinear optical phenomena under an intense light field [30] (see Section 2.1 in Methods). In the calculation, the laser power densities of 1.0×10^{12}, 1.0×10^{13}, 3.0×10^{13}, 5.0×10^{13}, and 1.0×10^{14} W/cm^2 corresponded to the maximum electric field amplitudes of 0.3, 0.9, 1.5, 0.9, and 2.7 V/Å, respectively. Owing to Fresnel reflection loss, the laser power density in the calculation was slightly higher than the actual experimental value. The polarization dependence of the time-integrated number of electrons $n_{ex}(t,\ \theta)$ excited at various laser power densities is shown in Fig. 1.

In the calculation, time integration was performed over a pulse width of 30 fs and normalized using the maximum value. The polarization direction θ corresponding to the electric field oscillating in the (111) plane shows the angle from the $[\bar{1}\bar{1}2]$ direction. Under excitation by a laser power density of 1.0×10^{12} W/cm^2 (Fig. 1(a)), no apparent polarization dependence was confirmed. Such results for a low laser power density are related to a previously reported calculation for diamond, in which the nonlinear response of the electronic excitation energy started at approximately 10^{13} W/cm^2 [18]. When the laser power density reached the level at which a nonlinear response could occur, two major factors were identified from these calculations. First, at the laser power density with an order of approximately 10^{13} W/cm^2, the $n_{ex}(t,\ \theta)$ has remarkable polarization dependence (Fig. 1(b–d)); this is consistent with the findings of the previous studies that showed the dependence of the effect of multiphoton absorption on the polarization state [25,26]. Moreover, the degree to which the $n_{ex}(t,\ \theta)$ varies with the polarization direction θ depends on the laser power density. This corresponds to the fact that the dominant ionization process changes from multiphoton to tunneling as the laser intensity increases [21,22]. When the laser power density exceeded 10^{14} W/cm^2, the degree of variation depending on the polarization direction decreased (Fig. 1(e)), implying that tunneling ionization became dominant. Secondly, the $n_{ex}(t,\ \theta)$ variation as a function of the polarization direction was changed by the laser power density; for instance, the graph for 1.0×10^{13} W/cm^2 was convex upward (Fig. 1(b)), whereas that for 5.0×10^{13} W/cm^2 was convex downward (Fig. 1(d)) for the same polarization direction of 30°. This is because the higher-order terms in the nonlinear interaction become more pronounced depending on the laser power density. Given the symmetry of the ground state of the diamond consisting of sp^3 hybridized carbon atoms, the response of electron excitation $n_{ex}(t,\ \theta)$ should be

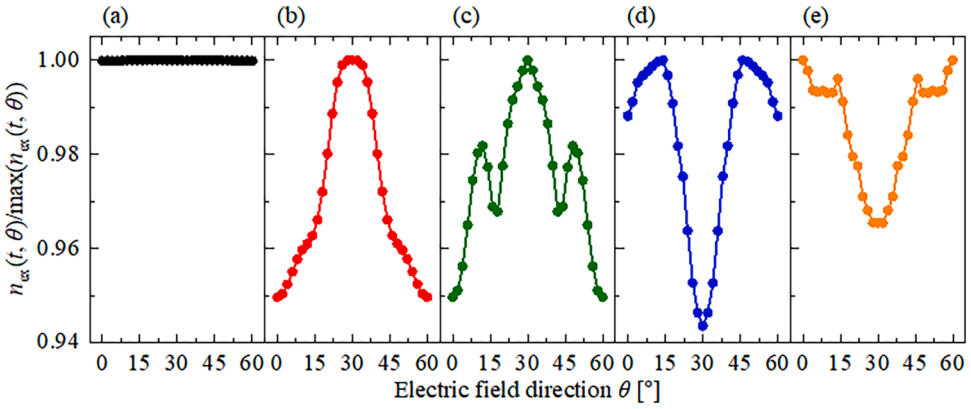

Fig. 1. Polarization-dependence of the number of excited electrons from TDDFT simulation. Polarization-dependence of the time-integrated number of electrons $n_{ex}(t,\ \theta)$ excited by the various laser power densities of (a) 1.0×10^{12} W/cm^2 (0.3 V/Å), (b) 1.0×10^{13} W/cm^2 (0.9 V/Å), (c) 3.0×10^{13} W/cm^2 (1.5 V/Å), (d) 5.0×10^{13} W/cm^2 (1.9 V/Å), and (e) 1.0×10^{14} W/cm^2 (2.7 V/Å). Time integration of $n_{ex}(t,\ \theta)$ is performed over a pulse width of 30 fs and normalized by the maximum value. The direction θ of the electric field oscillating in the (111) plane is the angle from the $[\bar{1}\bar{1}2]$ direction.

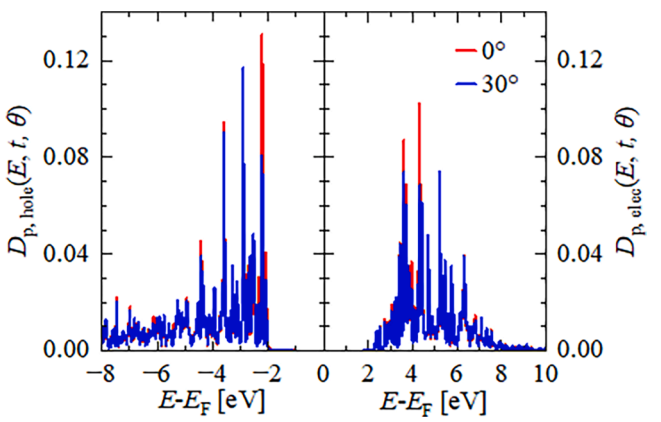

Fig. 2. Calculated carrier density of states (cDoS) of holes (left side) and electrons (right side) at 15 fs after excitation by the laser pulse with different polarization directions $\theta = 0°$ or 30° The Fermi level is set as the reference energy. The laser power density (maximum amplitude of the electric field) is 1.0×10^{13} W/cm^2 (0.9 V/Å).

polarization dependent with a period of 60°. However, at any laser power density, the calculated $n_{ex}(t,\ \theta)$ did not have a periodicity similar to a sinusoidal curve; however, it exhibited a complex dependence. Multiphoton ionization depends on the alignment of the crystal in the laser polarization direction, arising primarily from the anisotropy of the dynamic' effective mass [31]. As the effective mass is expressed as a second-order derivative of the band energy in reciprocal space, we calculated the polarization dependence of the excited carrier distribution.

The calculated career density of states (cDoS) of the excited electrons and holes at $t = 15$ fs calculated from Eqs. (4) and (5) are shown in Fig. 2. The laser power density and polarization direction were set to 1.0 $\times 10^{13}$ W/cm^2 and 0°/30°, respectively. The Fermi level was set as the reference energy. Comparing the energy level of the excited electrons, a higher energy level was occupied by the electrons excited in the polarization direction at 0°, even though the same laser power density was used, indicating that changes in the electronic occupation of the bands show polarization dependence.

To clarify the detailed changes in the electronic occupation of the bands after femtosecond laser excitation with various polarization directions, the cDoS of holes ($D_{p,\ hole}$) and electrons ($D_{p,\ elec}$) were calculated using Eqs. (4) and (5), respectively. The color maps for the cDoS as a function of the polarization direction are shown in Fig. 3. In this calculation, the laser power density was set to 1.0×10^{13} W/cm^2 or 3.0×10^{13} W/cm^2. The arrows with symbols for [E_{h1}–E_{h4}] and [E_{e1}–E_{e6}] indicate the selected main energy levels of [−4.4, −3.6, −2.9, −2.2] eV and [+3.6, +4.3, +4.7, +5.2, +5.8, +6.3] eV, respectively. The cDoS maps for 5.0×10^{13} and 1.0×10^{14} W/cm^2 are also shown in Supplementary Fig. S11. The electrons were excited to higher energy levels by the higher laser power density; however, the energy levels were not an indicator of the ease of excitation. In other words, the cDos values at lower energy levels were not necessarily at their maximum.

To investigate how the excited electrons occupy the bands and how the polarization direction affects the excitation in detail, we plotted the cDoS of the main energy levels as a function of the polarization direction (Fig. 4). The cDoS values at each energy level (E_{h1}–E_{h4} and E_{e1}–E_{e6} in Fig. 3) were integrated over a range of ±0.15 eV and averaged ($\widetilde{D}_{p,\ hole}$ and $\widetilde{D}_{p,\ elec}$). The plots for 5.0×10^{13} and 1.0×10^{14} W/cm^2 are shown in Supplementary Fig. S12. From these graphs, the variation in the cDoS value at each energy level implies a degree of polarization dependence. Focusing on the $\widetilde{D}_{p,\ hole}$, that is, the probability of electron escape, the degree of polarization dependence was remarkable for 1.0×10^{13} and 3.0×10^{13} W/cm^2. Particularly, the $\widetilde{D}_{p,\ hole}$ values for energy levels of E_{h4} (−2.4 – −2.1 eV) and E_{h3} (−3.0 – −2.7 eV) were substantially varied according to the polarization direction. For a laser power density higher

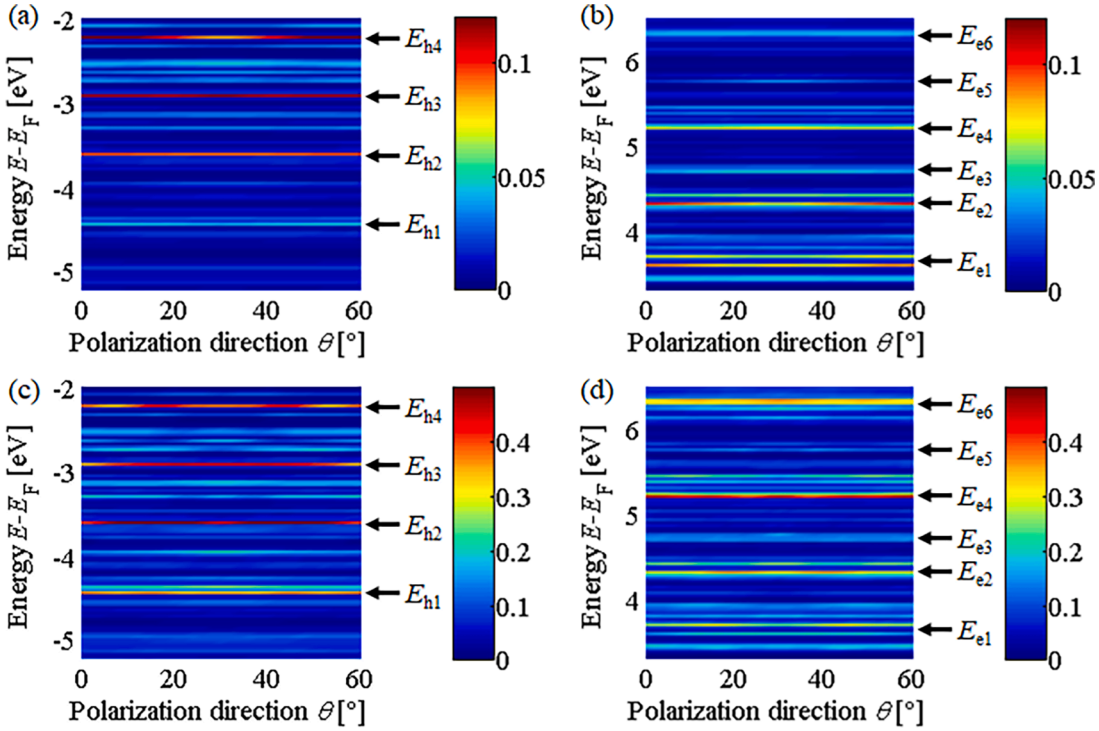

Fig. 3. Maps for the calculated cDoS of (a, c) holes $D_{p,\ hole}(E,t,\theta)$ and (b, d) electrons $D_{p,\ elec}(E,t,\theta)$ at 15 fs after excitation by the laser pulse with varying polarization direction θ. The laser power density (maximum amplitude of the electric field) is (a, b) 1.0×10^{13} W/cm^2 (0.9 V/Å) and (c, d) 3.0×10^{13} W/cm^2 (1.5 V/Å), respectively. The arrows with the symbols for (E_{h1}–E_{h4}) and (E_{e1}–E_{e6}) denote the selected main energy levels of (−4.4, −3.6, −2.9, −2.2) eV and (+3.6, +4.3, +4.7, +5.2, +5.8, +6.3) eV, respectively.

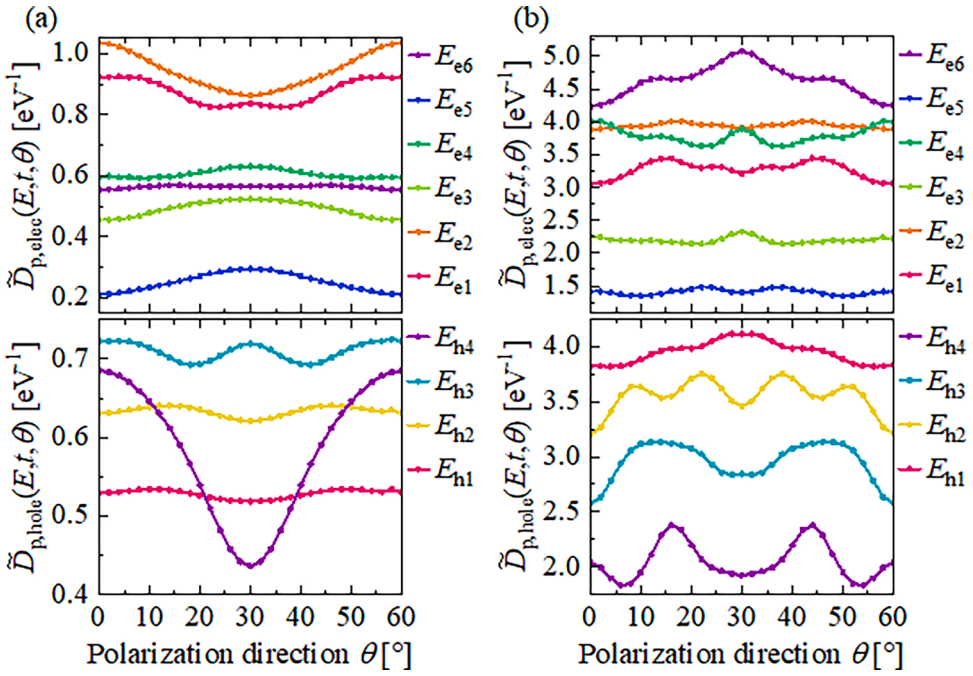

Fig. 4. Plots of the $D_{p,\ hole}$ (lower side) and the $D_{p,\ elec}$ (upper side) of the selected main energy levels from E_{h1} to E_{h4} and from E_{e1} to E_{e6} plotted in Fig. 3. The laser power density (maximum amplitude of the electric field) is (a) 1.0×10^{13} W/cm^2 (0.9 V/Å) and (b) 3.0×10^{13} W/cm^2 (1.5 V/Å) for E_{h1}–E_{h4} and E_{e1}–E_{e6}, respectively. In these plots, the cDoS values at each energy level (E_{h1}–E_{h4} and E_{e1}–E_{e6}) are integrated over a range of ±0.15 eV and averaged. The energy levels for (E_{h1}–E_{h4}) and (E_{e1}–E_{e6}) are (−4.4, −3.6, −2.9, −2.2) eV and (+3.6, +4.3, +4.7, +5.2, +5.8, +6.3) eV, respectively.

than 3.0×10^{13} W/cm^2, the degree of polarization dependence decreased and the larger $\tilde{D}_{p,\ hole}$ values were successively located from the deeper initial energy level.

However, the degree of polarization dependence of the $\tilde{D}_{p,\ elec}$ is complicated. For example, for a laser power density higher than 3.0×10^{13} W/cm^2, the $\tilde{D}_{p,\ elec}$ of E_{e6} (+6.2 – +6.5 eV) was the largest and easy to excite; in contrast, the $\tilde{D}_{p,\ elec}$ of E_{e5} (+5.7 – +6.0 eV) was difficult to excite for every laser power density. Furthermore, energy levels (E_{e1}: +3.5 – +3.8 eV, E_{e2}: +4.2 – +4.5 eV, and E_{e6}) with larger $\tilde{D}_{p,\ elec}$ appear to have a larger variation in $\tilde{D}_{p,\ elec}$ values, indicating that the degree of polarization dependence is larger. This polarization dependence is remarkable for 1.0×10^{13} and 3.0×10^{13} W/cm^2. The degree of the

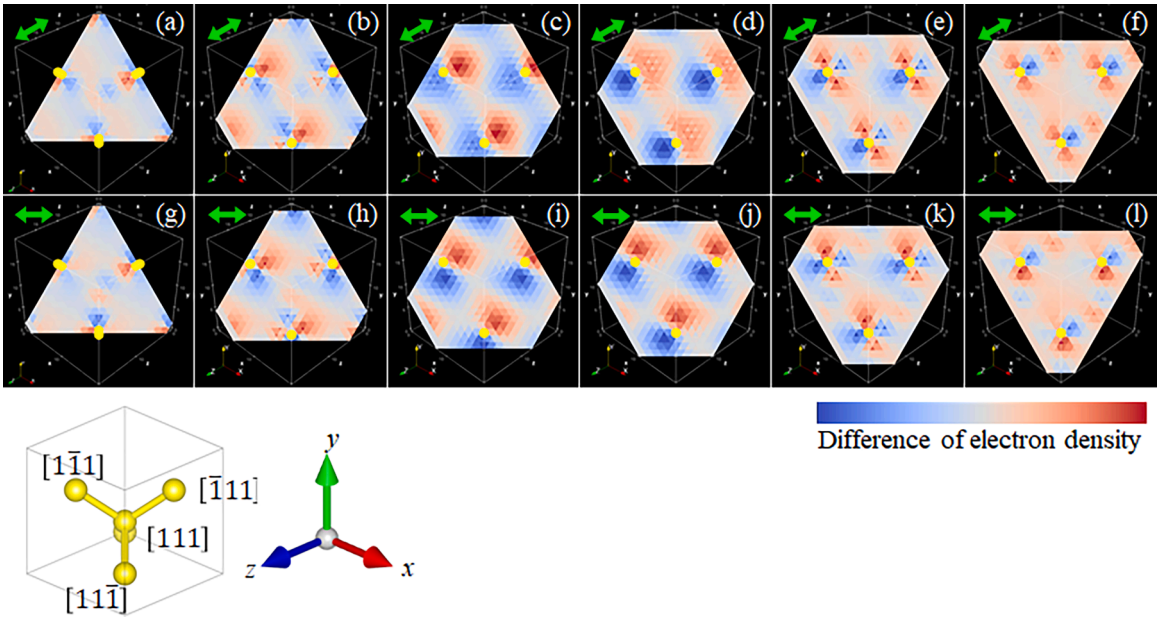

Fig. 5. Spatial distribution of the electron density in a view from $[\bar{1}\bar{1}\bar{1}]$ direction from TDDFT simulation. Spatial distribution of the difference of electron density from the ground state $d_{diff}(r,\ t)$ excited by an electric field of 1.0×10^{13} W/cm^2 with different polarization directions of (A–F) 0° or (G–L) 30° The spatial distribution of the electron density after 15 fs of excitation in a view from $[\bar{1}\bar{1}\bar{1}]$ direction is shown. There are six cross-sectional (111) planes with different distances from the origin. The green arrow and the yellow sphere show the polarization direction projected on the (111) plane and the carbon site, respectively. Schematic of four diamond crystallographic axes corresponding to the observation direction is also shown.

polarization dependence of $\widetilde{D}_{\mathrm{p,\ elec}}$ decreased as the laser power density increased, indicating that the dominant ionization process changed from multiphoton to tunneling (Fig. 4 and Supplementary S12). More interestingly, the degree of polarization dependence varied with the energy level even though the laser power density was the same, suggesting that electron excitation is sensitive to the polarization direction. These results indicate that the spatial distribution of excited electrons differs depending on the polarization direction and laser power density. Consequently, the change in the excited carrier distribution promotes the anisotropy of the effective mass according to the polarization direction, leading to the anisotropy of excitation in $[11\bar{1}]$, $[\bar{1}11]$, and $[1\bar{1}1]$ directions.

We also calculated the indirect contribution of excitation along the [111] direction based on the spatial distribution of the excited electrons. Based on Eq. (6), the spatial distribution of the difference in electron density from the ground state $d_{\mathrm{diff}}(\mathbf{r},\ t)$ excited by an electric field of 1.0 $\times 10^{13}$ W/cm^2 with different polarization directions of $\theta = 0°$ or 30° was calculated (Fig. 5). These figures show the spatial distribution of the electron density after 15 fs of excitation in a view from the $[\bar{1}\bar{1}\bar{1}]$ direction. The polarization direction is indicated by an arrow projected onto the (111) plane. There are six cross-sectional (111) planes at different distances from the origin along the [111] direction. The distance between the origin and cross-section (a) is 2.23 Å. The distance between the cross-sections increases by 0.309 Å from (a) to (f). In addition, a schematic of four diamond crystallographic axes corresponding to the direction of observation is shown.

For $\theta = 0°$, the electron density distribution was linearly symmetric in any cross-section with the direction of the polarization direction as the boundary. However, the electron density distribution was not linearly symmetric with respect to the polarization direction at 30° Such an asymmetric electron density distribution is prominently observed in Fig. 5(h–k). The electron density distributions in Fig. 5(i, j) and 5(h, k) appear to rotate anticlockwise and clockwise, respectively. In other words, for $\theta = 30°$, the electron-deficient region corresponding to the blue region is wiggly distributed along the [111] direction moving away from the origin. Such differences in the spatial electron density distribution along the [111] direction according to the polarization direction are attributed to the indirect effect of the anisotropy of excitation in the $[11\bar{1}]$, $[\bar{1}11]$, and $[1\bar{1}1]$ directions. Consequently, the polarization dependence of the NV axis orientation along the [111] direction appears.

Further, we performed a similar simulation of the spatial distribution of excited electrons in the (110) and $(1\bar{1}0)$ planes (Supplementary Figs. S13, S14). There were seven different cross-sections along [110] and $[1\bar{1}0]$ directions for each polarization direction. Similar to the observations in the cross-sectional (111) planes, the distribution of the electron density at 0° viewed from the [110] direction [Supplementary Fig. S13(a–g)] had symmetry in all cross-sections with respect to the polarization direction. However, the distribution of the electron density at 30° was inclined toward the $[1\bar{1}0]$ direction, and no significant distribution was observed in the $[\bar{1}10]$ direction [Supplementary Fig. S13(i, j)].

For the distribution of electron density viewed from the $[1\bar{1}0]$ direction, there were no significant differences in the spatial distribution in the cross-sections along the $[\bar{1}10]$ direction according to the polarization direction (Supplementary Fig. S14). In these calculations, the polarization direction for 0° lies in the plane including the bonds in the [111] and $[11\bar{1}]$ directions; for 30°, the polarization direction rotates toward the front of the page. Here, we focus on the electron distribution changes in the diamond crystallographic axes of $[11\bar{1}]$, $[\bar{1}11]$, and $[1\bar{1}1]$. The difference in electron density along the $[11\bar{1}]$ axis at 0° was slightly larger than that at 30° Comparing the electron density distributions of the cross-sections in [Supplementary Fig. S14(a, b, h, and i)] across the diamond crystallographic axis of $[\bar{1}11]$ and those for the cross-sections in [Supplementary Fig. S14(d, e, k, and l)] across the diamond crystallographic axis of $[1\bar{1}1]$, differences in electron density were observed depending on the polarization direction. It should be noted that the relative angle between the diamond crystallographic axis ($[\bar{1}11]$ or $[11\bar{1}]$) and the polarization direction is the same. Such polarization-dependent contributions to the electron density distribution in the diamond crystallographic axes of $[11\bar{1}]$, $[1\bar{1}1]$, and $[\bar{1}11]$ can indirectly affect the change in electron density along [111].

3.2. Analytical results of polarization-dependence of NV axes' orientation

By observing from the [110] direction, the directions of four NV axes in the single NV center have been classified into two groups—in-plane and out-of-plane. A previous study reported that a statistically significant bias was observed by terminating the annealing process with real-time feedback on the fluorescence intensity, although the reason for this is presently unknown [15]. In contrast, we focused on the orientation of the ensemble NVs without annealing. As the feasibility of the polarization dependence of electron excitation under an intense light field was confirmed by TDDFT calculations, we experimentally explored whether polarization dependence exists on the orientation of the axes of the ensemble NVs. In the experiments, we evaluated the polarization dependence of the orientation of the axes of ensemble NVs using two different methods. By irradiating femtosecond laser pulses along the [111] direction, the directions of four NV axes were distinguished from the [111] and the other three equivalent directions ($[11\bar{1}]$, $[\bar{1}11]$, and $[1\bar{1}1]$). After the formation of ensemble NVs via femtosecond laser irradiation without thermal annealing, the laser-processed regions were analyzed using two different methods—optical detected magnetic resonance (ODMR) and the fluorescence polarization microscope (FPM)—as described in Sections 2.5 and 2.6 in Methods. For direct writing of the ensemble NVs, we used femtosecond laser pulses with different polarization states—linear and circular (see Section 2.2 in Methods). Based on the fluorescence map of the sample including a set of

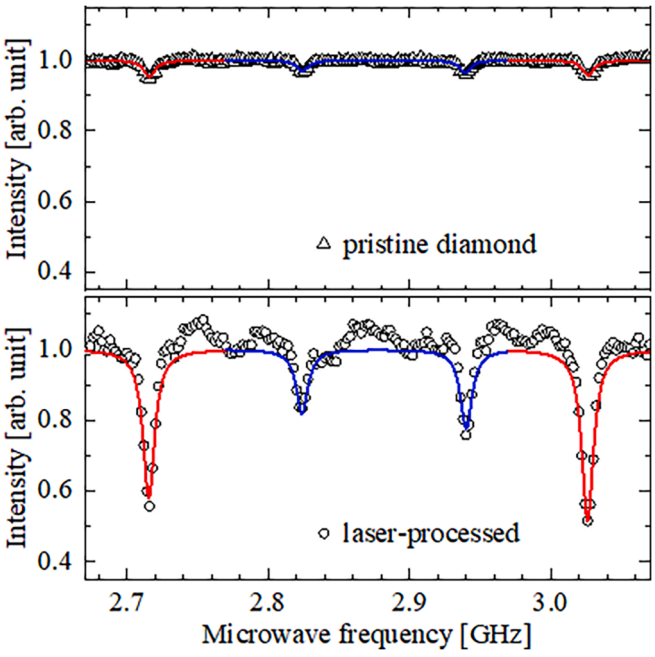

Fig. 6. Typical ODMR spectra of both the laser-processed region and the pristine diamond near the laser-processed region. ODMR spectrum of ensemble NVs at the region processed by femtosecond laser pulses with the polarization direction of $\theta = 66°$ ODMR spectrum at the pristine diamond near the laser-processed region is also shown. The red and blue curves show the fitted curves for the ODMR signals in the direction parallel to [111] and along the other three directions, respectively.

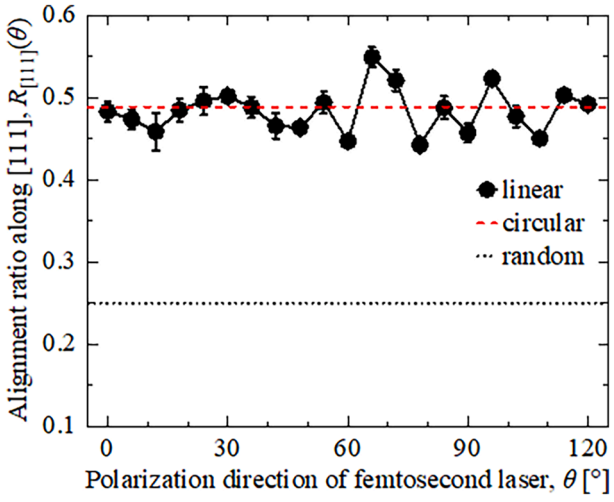

Fig. 7. Alignment ratio along [111] direction of ensemble NVs obtained by ODMR measurements. Alignment ratio along [111]direction of ensemble NVs formed by the femtosecond laser pulses with various polarization states propagating along [111] direction. The $R_{[111]}(\theta)$ values as a function of linear polarization direction θ in the (111) plane were calculated by using $k(\theta) = 1.4$. Typical $R_{[111]}$ values for circular polarization (red dashed line) is also shown. The black dotted line shows the $R_{[111]}$ value for random orientation.

laser-processed regions (Fig. S1), we set the measurement position for ODMR. Typical ODMR spectra of both the laser-processed region for the polarization direction of $\theta = 54°$ and the pristine diamond near the laser-processed region are shown in Fig. 6. The ODMR signals at the laser-processed region were substantially dropped compared to those for the pristine diamond.

3.3. Alignment ratio along the [111] NV axis

The alignment ratio along the [111] direction $R_{[111]}(\theta)$ identified by the ODMR measurements is plotted in Fig. 7. In this figure, the $R_{[111]}(\theta)$ values obtained using femtosecond laser pulses with not only linear polarization but also circular polarization are shown. The concentration of ensemble NVs after the laser irradiation was estimated as 6×10^{14} cm^{-3} by normalizing with the fluorescence intensity of a single NV center in the confocal volume [32]. Here we define the upper bound of the alignment ratio along the [111] direction using Eq. (7) with $k(\theta) = 1.4$ [39]. The rise in $R_{[111]}(\theta)$ value up to 0.55 after the femtosecond laser irradiation for a certain polarization direction $\theta = 66°$ compared to that of the random orientation. This corresponds to an increase of 30 % in contrast to the optically magnetic resonance signal with 0.25 for random orientation. This results in a 30 % enhancement in the sensitivity of the quantum sensor because the contrast is linearly proportional to the sensitivity below the shot-noise limit [7].

Considering that the originally existing NV axis orientation in the pristine diamond is random, the alignment ratio along the [111] direction $R^{pristine}_{[111]}(\theta)$ should be 0.25. Therefore, we can obtain the $k(\theta)$ value by $k(\theta) = 3S^{pristine}_{[111]}(\theta)/S^{pristine}_{others}(\theta)$. We measured the ODMR signals at the position 5 μm away from each laser-processed region (Supplementary Figs. S2−S4) and obtained $S^{pristine}_{[111]}(\theta)$ and $S^{pristine}_{others}(\theta)$. Unexpectedly, the $R^{pristine}_{[111]}(\theta)$ $(= S^{pristine}_{[111]}(\theta)/\{S^{pristine}_{[111]}(\theta) + 3S^{pristine}_{others}(\theta)\})$ varied depending on the measurement positions even in the pristine diamond, which could be due to the biased orientation in the low NV concentration ($\sim 6 \times 10^{13}$ cm^{-3}). Therefore, we plotted the empirical parameter of $k(\theta)$ from the ODMR signals obtained by the pristine diamond at each measurement position in Supplementary Fig. S15. As previously reported [39], the empirical parameter of $k(\theta)$ should be carefully determined. Here we calculated $R_{[111]}(\theta)$ using $k(\theta)$ values determined by three different methods. In Fig. 7, each $R_{[111]}(\theta)$ for $k(\theta) = 1.4$ was calculated, considering the microwave application method [39]. In this case, the upper bound of $R_{[111]}(\theta)$ reached the maximum of 0.55 at $\theta = 66°$. Furthermore, $R_{[111]}(\theta)$ was calculated from each $k(\theta)$ value for the pristine diamond 5 μm away from each laser-processed region (Supplementary Fig. S16). Considering the randomness of the NV axes orientation in the diamond sample synthesized without control of crystallographic orientations, the average of $R^{pristine}_{[111]}(\theta)$ at each measurement position should be 0.25. A good fitting result of the averaged $R^{pristine}_{[111]}(\theta) = 0.25$ was obtained when $k(\theta) = 3.6$. We also calculated $R_{[111]}(\theta)$ for $k(\theta) = 3.6$ (Supplementary Fig. S17). In this case, the $R_{[111]}(\theta)$ only increased to 0.32 at $\theta = 66°$, corresponding to a slight enhancement (7 %) of the [111] orientation of ensemble NVs. The correlation plot between $k(\theta)$ and $R_{[111]}(\theta)$ (Supplementary Fig. S18) indicates negative correlation between these values. This indicates that the increasing rate of $R_{[111]}(\theta)$ after the laser irradiation is larger, as the alignment ratio along the [111] direction of the pristine NV axis is smaller. The $R_{[111]}(\theta)$ is in a range from 32 % ($k(\theta) = 3.6$) to 55 % ($k(\theta) = 1.4$). Currently, no firm conclusion was reached regarding the suitable value of $k(\theta)$ for the $R_{[111]}(\theta)$ calculation. Therefore, a more detailed investigation is necessary.

In all plots of $R_{[111]}(\theta)$ (Fig. 7, Supplementary S16 and S17), by rotating the linear polarization direction θ in the (111) plane, the $R_{[111]}(\theta)$ value for the linear polarization appeared to oscillate around that for the circular polarization. This result can be interpreted based on the fact that the time-averaged electric field of the circular polarization oscillates in all directions in the (111) plane.

3.4. Polarization-dependence of the orientation of NV axes

Typical plots of the FPM observations of the laser-processed region for the linear polarization direction $\theta = 90°$ are shown in Fig. 8. In this figure, the obtained normalized intensities $I_r(90°, \phi)$ by rotating the polarization direction ϕ of the excited green laser are fitted using Eq. (9). The red curve shows the fitting function of $I_r(90°, \phi) = A_0(90°) + A_1(90°)\cos 2(\phi - \phi_c(90°))$. Using the fitting parameters of $A_0(90°)$, $A_1(90°)$, and $\phi_c(90°)$, we calculated $a(90°)$, $b(90°)$, $c(90°)$, $d(90°)$, and $r_i(90°)$ using Eqs. (10–18). Calculating these values for other values of polarization θ can clarify the relationship between the polarization direction of the femtosecond laser and the orientation of the NV axes.

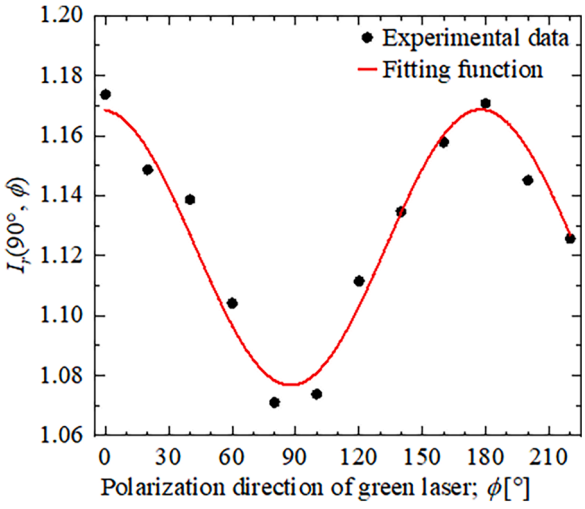

Fig. 8. Typical plots from FPM observation of the laser-processed region for the linear polarization direction $\theta = 90°$ The red curve shows the fitting function of $I_r(90°, \phi) = A_0(90°) + A_1(90°)\cos 2(\phi - \phi_c(90°))$.

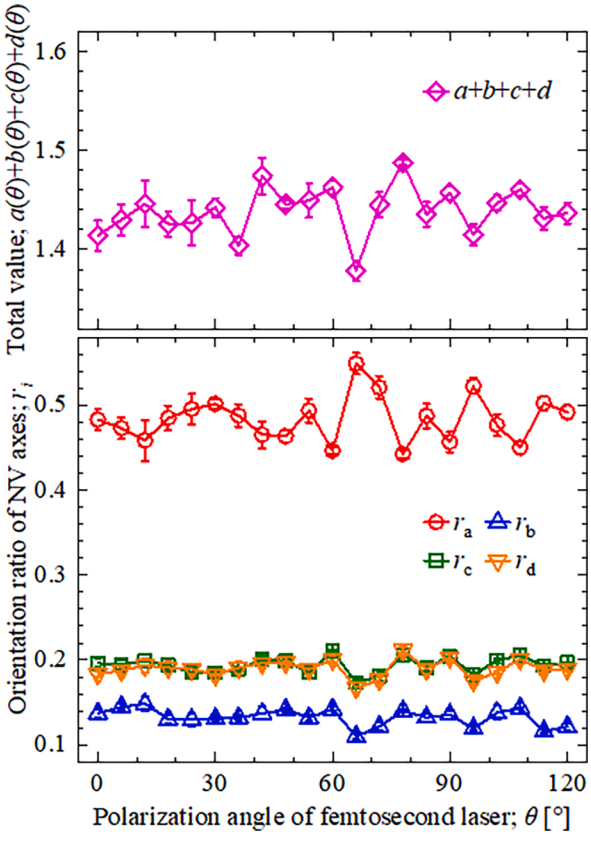

Fig. 9. Alignment ratio along the four NV axes' directions calculated from FPM measurements. Plots of $r_i(\theta)$ and the total value of $a(\theta) + b(\theta) + c(\theta) + d(\theta)$ as a function of the polarization direction θ for NV formation. It should be noted that the values of r_a, r_b, r_c, and r_d represent the alignment ratio along the [111], [11$\bar{1}$], [$\bar{1}$11], and [1$\bar{1}$1] directions, respectively.

Fig. 9 shows plots of $r_i(\theta)$ and the total value of $a(\theta) + b(\theta) + c(\theta) + d(\theta)$ as a function of the polarization direction θ for NV formation. The values of r_a, r_b, r_c, and r_d represent the alignment ratios along the [111], [11$\bar{1}$], [$\bar{1}$11], and [1$\bar{1}$1] planes, respectively. The total value indicating the number of NV centers formed by femtosecond laser irradiation changed with the polarization direction. When the r_a value increased, r_b, r_c, r_d, and the total value decreased. The trends of variations in r_b, r_c, and r_d according to the polarization direction were similar. The fact that the increase in r_a corresponds to a decrease in the total value indicates that the migration of carbon atoms along the [111] direction is promoted more than that along the other three directions. Although the alignment ratio along the [111] direction showed a polarization dependence, no apparent polarization dependence was observed for the other three directions ([11$\bar{1}$], [$\bar{1}$11], and [1$\bar{1}$1]). Although previous studies have revealed that the light-matter interaction changes depending on the crystal symmetry [25], no apparent differences in the polarization dependence of the r_b, r_c, and r_d are observed. A negative correlation between NV concentration and $R_{[111]}$ from Fig. 9 intuitively indicates that with the polarization inducing [111] alignment, the NV formation along the other three directions does not likely occur. No major difference in the trends for the other three directions ([11$\bar{1}$], [$\bar{1}$11], and [1$\bar{1}$1]) also indicates that the NV centers along [111] direction are efficiently formed under a certain polarization condition.

4. Discussion

Although the TDDFT calculations indicate that the polarization dependence of the electron excitation under an intense light field can lead to polarization dependence on the orientation of the axes of the ensemble NVs, no apparent polarization dependence is experimentally observed for the three directions ([11$\bar{1}$], [$\bar{1}$11], and [1$\bar{1}$1]), except for the enhancement of the [111] orientation of the ensemble NVs. There are two possible reasons for this. First, the atomic migration induced by thermalization after laser irradiation is also a key factor in NV formation. Optimizing the laser parameters by shortening the pulse width and minimizing the number of irradiation pulses results in polarization dependence during NV formation. Furthermore, the pulse repetition rate is also essential, even though heat accumulation is expected to be negligible under our experimental conditions owing to the rapid thermal diffusivity of diamond. Indeed, we recently confirmed that the formation efficiency of NV centers depends on the pulse repetition rate [18]. The changes in the absorption of laser energy or the distortion of the diamond lattice during laser irradiation should be clarified.

The second is the complex periodicity or aperiodicity of the effective mass of excited electrons with respect to the polarization direction. Previous studies have reported that multiphoton ionization rates [25] and Keldysh parameters [21,33] are affected by the anisotropy in the effective mass of the excited electrons. The periodicity of the direction between the G and K points with good symmetry, similar to that of the M and K points, corresponds to the polarization dependence of the light-matter interaction [25]. According to the coordinates of all X, L, W, U, and K points in the Brillouin zone projected onto the (111) plane (Supplementary Fig. S19), the periodicity in the direction between the G point corresponding to the origin and each coordinate point is complicated, particularly at the W and U points. This complexity is one of the reasons for the complex polarization dependence of NV formation observed in the experiments. Although the TDDFT calculations showed different interactions among the [11$\bar{1}$], [$\bar{1}$11], and [1$\bar{1}$1] directions, we could not observe clear differences in orientation among these directions other than the [111] direction.

5. Conclusions

We concluded that although the polarization dependence of the NV axis orientation along the [111] direction appeared to have periodicity, this phenomenon occurred owing to the indirect results from the anisotropy of the electron excitation in the [11$\bar{1}$], [$\bar{1}$11], and [1$\bar{1}$1] directions. Based on the TDDFT simulation results, we gain valuable insights into the significance of polarization direction in nonlinear light-matter interaction. These findings hold great relevance for the field of quantum optics. In contrast to the previous studies for the orientation of the single NV [15], the statistical control for the ensemble NVs will be more complicated due to the multi-body problem.

Apart from understanding the underlying mechanism, the experimental fact that the alignment ratio along the direction parallel to [111] increased to 55 % by the simple method of just laser irradiation is surprising. Thus far, we have reported characteristic functions induced by the femtosecond laser direct-writing technique without any thermal process such as microscopic phase transformation into graphite with electric conductivity [34], formation of a large number of NV ensembles ($\sim 3 \times 10^{16}$ cm^{-3}) without degradation of their spin coherence time (T_2 for pristine diamond: $\sim$ 1.6 μs, T_2 after laser-processing: $\sim$ 2.4 μs) [17] and the diamond crystallinity [18]. However, although the preferential orientation of NV ensembles was restricted due to low NV concentration in the present experiments, we anticipate these insights may inspire approaches to boost the formation of quantum sensing devices by laser processing.

Data access

Additional data could be provided by the authors upon special request.

CRediT authorship contribution statement

Kohei Kinouchi: Formal analysis, Investigation, Methodology, Writing – original draft. **Yasuhiko Shimotsuma:** Conceptualization, Project administration, Investigation, Writing – review & editing, Funding acquisition. **Mitsuharu Uemoto:** Methodology, Investigation. **Masanori Fujiwara:** Methodology, Investigation. **Norikazu Mizuochi:** Methodology, Investigation. **Masahiro Shimizu:** Conceptualization, Investigation. **Kiyotaka Miura:** Project administration, Conceptualization, Investigation.

Declaration of Competing Interest

The authors declare that they have no known competing financial interests or personal relationships that could have appeared to influence the work reported in this paper.

Data availability

Data will be made available on request.

Acknowledgments

The computation in this study was performed using the supercomputer Oakforest-PACS at JCAHPC through the Multidisciplinary Cooperative Research Program in CCS, University of Tsukuba. This project received funding from the following sources: JSPS KAKENHI Grant No. 20H02656; MEXT Q-LEAP (JPMXS0118067395); Spintronics Research Network of Japan.

Supplementary materials

Supplementary material associated with this article can be found, in the online version, at doi:10.1016/j.cartre.2023.100318.

References

[1] G.D. Fuchs, G. Burkard, P.V. Klimov, D.D. Awschalom, A quantum memory intrinsic to single nitrogen–vacancy centres in diamond, Nat. Phys. 7 (2011) 789–793, https://doi.org/10.1038/nphys2026.
[2] E.D. Herbschleb, H. Kato, Y. Maruyama, T. Danjo, T. Makino, S. Yamasaki, I. Ohki, K. Hayashi, H. Morishita, M. Fujiwara, N. Mizuochi, Ultra-long coherence times amongst room-temperature solid-state spins, Nat. Commun. 10 (2019) 3766, https://doi.org/10.1038/s41467-019-11776-8.
[3] F. Jelezko, T. Gaebel, I. Popa, M. Domhan, A. Gruber, J. Wrachtrup, Observation of coherent oscillation of a single nuclear spin and realization of a two-Qubit conditional quantum gate, Phys. Rev. Lett. 93 (2004), 130501, https://doi.org/10.1103/PhysRevLett.93.130501.
[4] A. Beveratos, R. Brouri, T. Gacoin, A. Villing, J.P. Poizat, P. Grangier, Single photon quantum cryptography, Phys. Rev. Lett. 89 (2002), 187901, https://doi.org/10.1103/PhysRevLett.89.187901.
[5] N. Mizuochi, T. Makino, H. Kato, D. Takeuchi, M. Ogura, H. Okushi, M. Nothaft, P. Neumann, A. Gali, F. Jelezko, J. Wrachtrup, S. Yamasaki, Electrically driven single-photon source at room temperature in diamond, Nat. Photonics 6 (2012) 299–303, https://doi.org/10.1038/nphoton.2012.75.
[6] V.M. Acosta, E. Bauch, M.P. Ledbetter, C. Santori, K.-M.C. Fu, P.E. Barclay, R. G. Beausoleil, H. Linget, J.F. Roch, F. Treussart, S. Chemerisov, W. Gawlik, D. Budker, Diamonds with a high density of nitrogen-vacancy centers for magnetometry applications, Phys. Rev. B 80 (2009), 115202, https://doi.org/10.1103/PhysRevB.80.115202.
[7] J.M. Taylor, P. Cappellaro, L. Childress, L. Jiang, D. Budker, P.R. Hemmer, A. Yacoby, R. Walsworth, M.D. Lukin, High-sensitivity diamond magnetometer with nanoscale resolution, Nat. Phys. 4 (2008) 810–816, https://doi.org/10.1038/nphys1075.
[8] O.R. Rubinas, V.V. Vorobyov, V.V. Soshenko, S.V. Bolshedvorskii, V.N. Sorokin, A. N. Smolyaninov, V.G. Vins, A.P. Yelisseyev, A.V. Akimov, Spin properties of NV centers in high-pressure, high-temperature grown diamond, J. Phys. Commun. 2 (2018), 115003, https://doi.org/10.1088/2399-6528/aae992.
[9] L.M. Pham, N. Bar-Gill, D.Le Sage, C. Belthangady, A. Stacey, M. Markham, D. J. Twitchen, M.D. Lukin, R.L. Walsworth, Enhanced metrology using preferential orientation of nitrogen-vacancy centers in diamond, Phys. Rev. B 86 (2012), 121202, https://doi.org/10.1103/PhysRevB.85.121202.
[10] M. Capelli, A.H. Heffernan, T. Ohshima, H. Abe, J. Jeske, A. Hope, A.D. Greentree, P. Reineck, B.C. Gibson, Increased nitrogen-vacancy centre creation yield in diamond through electron beam irradiation at high temperature, Carbon 143 (2019) 714–719, https://doi.org/10.1016/j.carbon.2018.11.051.
[11] S. Pezzagna, B. Naydenov, F. Jelezko, J. Wrachtrup, J. Meijer, Creation efficiency of nitrogen-vacancy centres in diamond, New J. Phys. 12 (2010), 065017, https://doi.org/10.1088/1367-2630/12/6/065017.
[12] M. Haruyama, S. Onoda, T. Higuchi, W. Kada, A. Chiba, Y. Hirano, T. Teraji, R. Igarashi, S. Kawai, H. Kawarada, Y. Ishii, R. Fukuda, T. Tanii, J. Isoya, T. Ohshima, O. Hanaizumi, Triple nitrogen-vacancy centre fabrication by C5N4Hn ion implantation, Nat. Commun. 10 (2019) 2664, https://doi.org/10.1038/s41467-019-10529-x.
[13] T. Fukui, Y. Doi, T. Miyazaki, Y. Miyamoto, H. Kato, T. Matsumoto, T. Makino, S. Yamasaki, R. Morimoto, N. Tokuda, M. Hatano, Y. Sakagawa, H. Morishita, T. Tashima, S. Miwa, Y. Suzuki, N. Mizuochi, Perfect selective alignment of nitrogen-vacancy centers in diamond, Appl. Phys. Express. 7 (2014), 055201, https://doi.org/10.7567/APEX.7.055201.
[14] G.W (M.E. Newton, Morley) Y.C. Chen, P.S. Salter, S. Knauer, L. Weng, A. C. Frangeskou, C.J. Stephen, S.N. Ishmael, P.R. Dolan, S. Johnson, B.L. Green, J. G. Rarity, M.J. Booth, J.M. Smith, Laser writing of coherent colour centres in diamond, Nat. Photnics 11 (2017) 77–80, https://doi.org/10.1038/nphoton.2016.234.
[15] Y.C. Chen, B. Griffiths, L. Weng, S.S. Nicley, S.N. Ishmael, Y. Lekhai, S. Johnson, C. J. Stephen, B.L. Green, G.W. Morley, M.E. Newton, M.J. Booth, P.S. Salter, J. M. Smith, Laser writing of individual nitrogen-vacancy defects in diamond with near-unity yield, Optica 6 (2019) 662–667, https://doi.org/10.1364/DP.2019.28.
[16] T. Kurita, N. Mineyuki, Y. Shimotsuma, M. Fujiwara, N. Mizuochi, M. Shimizu, K. Miura, Efficient generation of nitrogen-vacancy center inside diamond with shortening of laser pulse duration, Appl. Phys. Lett. 113 (2018), 211102, https://doi.org/10.1063/1.5054730.
[17] T. Kurita, Y. Shimotsuma, M. Fujiwara, M. Fujie, N. Mizuochi, M. Shimizu, K. Miura, Direct writing of high-density nitrogen-vacancy centers inside diamond by femtosecond laser irradiation, Appl. Phys. Lett. 118 (2021), 214001, https://doi.org/10.1063/5.0049953.
[18] Y. Shimotsuma, K. Kinouchi, R. Yanoshita, M. Fujiwara, N. Mizuochi, M. Uemoto, M. Shimizu, K. Miura, Formation of NV centers in diamond by a femtosecond laser single pulse, Opt. Express. 31 (2023) 1594–1603, https://doi.org/10.1364/oe.475917.
[19] M. Fujiwara, S. Inoue, S. Masuno, H. Fu, S. Tokita, M. Hashida, N. Mizuochi, Creation of NV centers over a millimeter-sized region by intense single-shot ultrashort laser irradiation, APL Photon 8 (2023), 036108, https://doi.org/10.1063/5.0137093.
[20] S. Lagomarsino, S. Sciortino, B. Obreshkov, T. Apostolova, C. Corsi, M. Bellini, E. Berdermann, C.J. Schmidt, Photoionization of monocrystalline CVD diamond irradiated with ultrashort intense laser pulse, Phys. Rev. B. 93 (2016), 085128, https://doi.org/10.1103/PhysRevB.93.085128.
[21] L.V. Keldysh, Ionization in the field of a strong electromagnetic wave, Sov. Phys. JETP. 20 (1965) 1307–1314.
[22] A. Yamada, K. Yabana, Energy transfer from intense laser pulse to dielectrics in time-dependent density functional theory, Eur. Phys. J. D 73 (2019) 87, https://doi.org/10.1140/epjd/e2019-90334-7.
[23] S. Klarsfeld, A. Maquet, Circular versus linear polarization in multiphoton ionization, Phys. Rev. Lett. 29 (1972) 79–81, https://doi.org/10.1103/PhysRevLett.29.79.
[24] J. Muth-Böhm, A. Becker, F.H.M. Faisal, Suppressed molecular ionization for a class of diatomics in intense femtosecond laser fields, Phys. Rev. Lett. 85 (2000) 2280–2283, https://doi.org/10.1103/physrevlett.85.2280.
[25] M. Gertsvolf, H. Jean-Ruel, P.P. Rajeev, D.D. Klug, D.M. Rayner, P.B. Corkum, Orientation-dependent multiphoton ionization in wide band gap crystals, Phys. Rev. Lett. 101 (2008), 243001, https://doi.org/10.1103/PhysRevLett.101.243001.
[26] E.F. Martynovich, V.P. Dresvyansky, A.L. Rakevich, N.L. Lazareva, M. A. Arsentieva, A.A. Tyutrin, O. Bukhtsoozh, S. Enkhbat, P.V. Kostryukov, B. E. Perminov, A.V. Konyashchenko, Creating of luminescent defects in crystalline media by a scanning laser beam, Appl. Phys. Lett. 114 (2019), 121901, https://doi.org/10.1063/1.5087688.
[27] Y. Shimotsuma, P.G. Kazansky, J. Qiu, K. Hirao, Self-organized nanogratings in glass irradiated by ultrashort light pulses, Phys. Rev. Lett. 91 (2003), 247405, https://doi.org/10.1103/PhysRevLett.91.247405.
[28] M. Sakakura, Y. Lei, L. Wang, Y.H. Yu, P.G. Kazansky, Ultralow-loss geometric phase and polarization shaping by ultrafast laser writing in silica glass, Light Sci. Appl. 9 (2020) 15, https://doi.org/10.1038/s41377-020-0250-y.
[29] E.M. Dianov, P.G. Kazansky, D.Yu. Stepanov, Photoinduced effects in optical waveguides, SPIE Proc. 1516 (1991) 81–98, https://doi.org/10.1117/12.51150.
[30] M. Uemoto, S. Kurata, N. Kawaguchi, K. Yabana, First-principles study of ultrafast and nonlinear optical properties of graphite thin films, Phys. Rev. B 103 (2021), 085433, https://doi.org/10.1103/PhysRevB.103.085433.
[31] M. Kozák, T. Otobe, M. Zukerstein, F. Trojánek, P. Malý, Anisotropy and polarization dependence of multiphoton charge carrier generation rate in diamond, Phys. Rev. B 99 (2019), https://doi.org/10.1103/PhysRevB.99.104305.
[32] K. Hayashi, Y. Matsuzaki, T. Ashida, S. Onoda, H. Abe, T. Ohshima, M. Hatano, T. Taniguchi, H. Morishita, M. Fujiwara, N. Mizuochi, Experimental and theoretical analysis of noise strength and environmental correlation time for ensembles of nitrogen-vacancy centers in diamond, J. Phys. Soc. Jpn. 89 (2020), 054708, https://doi.org/10.7566/JPSJ.89.054708.

[33] A. Kaiser, B. Rethfeld, M. Vicanek, G. Simon, Microscopic processes in dielectrics under irradiation by subpicosecond laser pulses, Phys. Rev. B 61 (2000) 11437–11450, https://doi.org/10.1103/PhysRevB.61.11437.
[34] M. Shimizu, Y. Shimotsuma, M. Sakakura, T. Yuasa, H. Homma, Y. Minowa, K. Tanaka, K. Miura, K. Hirao, Periodic metallo-dielectric structure in diamond, Opt. Express 17 (2009) 46–54, https://doi.org/10.1364/oe.17.000046.
[35] M. Noda, S.A. Sato, Y. Hirokawa, M. Uemoto, T. Takeuchi, S. Yamada, A. Yamada, Y. Shinohara, M. Yamaguchi, K. Iida, I. Floss, T. Otobe, K.M. Lee, K. Ishimura, T. Boku, G.F. Bertsch, K. Nobusada, K. Yabana, SALMON: scalable ab-initio light–matter simulator for optics and nanoscience, Comput. Phys. Commun. 235 (2019) 356–365, https://doi.org/10.1016/j.cpc.2018.09.018.
[36] N. Troullier, J.L. Martins, Efficient pseudopotentials for plane-wave calculations, Phys. Rev. B Condens. Matter 43 (1991) 1993–2006, https://doi.org/10.1103/PhysRevB.43.1993.
[37] J.P. Perdew, A. Zunger, Self-interaction correction to density-functional approximations for many-electron systems, Phys. Rev. B 23 (1981) 5048–5079, https://doi.org/10.1103/PhysRevB.23.5048.
[38] M. Wu, D.A. Browne, K.J. Schafer, M.B. Gaarde, Multilevel perspective on high-order harmonic generation in solids, Phys. Rev. A 94 (2016), 063403, https://doi.org/10.1103/PhysRevA.94.063403.
[39] K. Tahara, H. Ozawa, T. Iwasaki, N. Mizuochi, M. Hatano, Quantifying selective alignment of ensemble nitrogen-vacancy centers in (111) diamond, Appl. Phys. Lett. 107 (2015), 193110, https://doi.org/10.1063/1.4935709.
[40] R.J. Epstein, F.M. Mendoza, Y.K. Kato, D.D. Awschalom, Anisotropic interactions of a single spin and dark-spin spectroscopy in diamond, Nat. Phys. 1 (2005) 94–98, https://doi.org/10.1038/nphys141.
[41] Y. Kubo, F.R. Ong, P. Bertet, D. Vion, V. Jacques, D. Zheng, A. Dréau, J.F. Roch, A. Auffeves, F. Jelezko, J. Wrachtrup, M.F. Barthe, P. Bergonzo, D. Esteve, Strong coupling of a spin ensemble to a superconducting resonator, Phys. Rev. Lett. 105 (2010), 140502, https://doi.org/10.1103/PhysRevLett.105.140502.